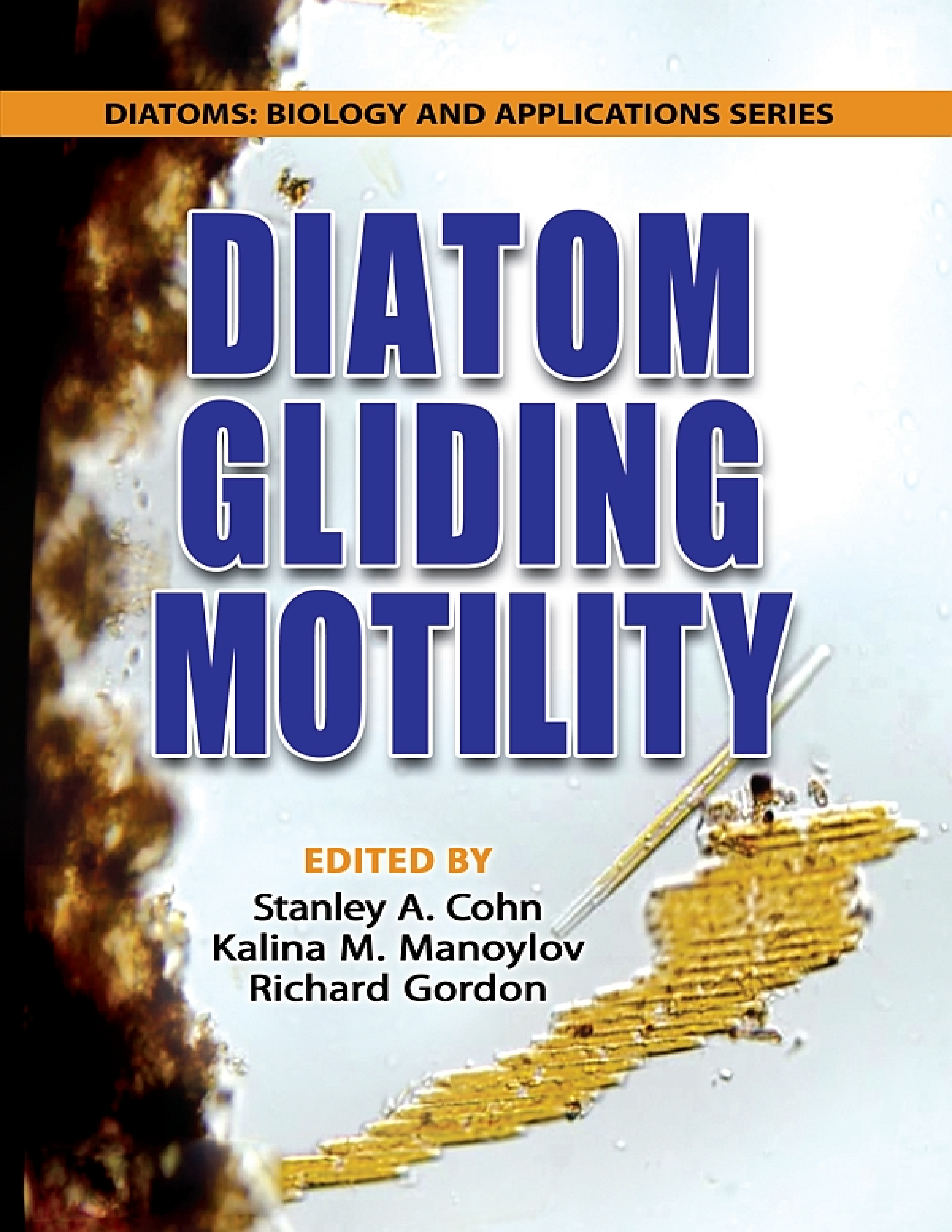

DIATOMS: BIOLOGY AND APPLICATIONS SERIES

DIATOM GLIDING MOTILITY

EDITED BY
Stanley A. Cohn
Kalina M. Manoylov
Richard Gordon

Table of Contents

- Cover
- Title Page
- Copyright
- Dedication to Jeremy D. Pickett-Heaps In Memoriam 1940–2021
- Preface
- 1 Some Observations of Movements of Pennate Diatoms in Cultures and Their Possible Interpretation
    - 1.1 Introduction
    - 1.2 Kinematics and Analysis of Trajectories in Pennate Diatoms with Almost Straight Raphe along the Apical Axis
    - 1.3 Curvature of the Trajectory at the Reversal Points
    - 1.4 Movement of Diatoms in and on Biofilms
    - 1.5 Movement on the Water Surface
    - 1.6 Formation of Flat Colonies in C*ymbella lanceolata*
    - 1.7 Conclusion
    - References
- 2 The Kinematics of Explosively Jerky Diatom Motility: A Natural Example of Active Nanofluidics
    - 2.1 Introduction
    - 2.2 Material and Methods
    - 2.3 Results and Discussion
    - 2.4 Conclusions
    - Appendix

- References

3 Cellular Mechanisms of Raphid Diatom Gliding
- 3.1 Introduction
- 3.2 Gliding and Secretion of Mucilage
- 3.3 Cell Mechanisms of Mucilage Secretion
- 3.4 Mechanisms of Gliding Regulation
- 3.5 Conclusions
- Acknowledgments
- References

4 Motility of Biofilm-Forming Benthic Diatoms
- 4.1 Introduction
- 4.2 General Motility Models and Concepts
- 4.3 Light-Directed Vertical Migration
- 4.4 Stimuli-Directed Movement
- 4.5 Conclusion
- References

5 Photophobic Responses of Diatoms – Motility and Inter-Species Modulation
- 5.1 Introduction
- 5.2 Types of Observed Photoresponses
- 5.3 Inter-Species Effects of Light Responses
- 5.4 Summary
- References

6 Diatom Biofilms: Ecosystem Engineering and Niche Construction
- 6.1 Introduction
- 6.2 The Microphytobenthos and Epipelic Diatoms
- 6.3 The Ecological Importance of Locomotion
- 6.4 Ecosystem Engineering and Functions

  - 6.5 Microphytobenthos as Ecosystem Engineers
  - 6.6 Niche Construction and Epipelic Diatoms
  - 6.7 Conclusion
  - Acknowledgments
  - References
- 7 Diatom Motility: Mechanisms, Control and Adaptive Value
  - 7.1 Introduction
  - 7.2 Forms and Mechanisms of Motility in Diatoms
  - 7.3 Controlling Factors of Diatom Motility
  - 7.4 Adaptive Value and Consequences of Motility
  - Acknowledgments
  - References
- 8 Motility in the Diatom Genus *Eunotia* Ehrenb.
  - 8.1 Introduction
  - 8.2 Accounts of Movement in *Eunotia*
  - 8.3 Motility in the Context of Valve Structure
  - 8.4 Motility and Ecology of *Eunotia*
  - 8.5 Motility and Diatom Evolution
  - 8.6 Conclusion and Future Directions
  - Acknowledgements
  - References
- 9 A Free Ride: Diatoms Attached on Motile Diatoms
  - 9.1 Introduction
  - 9.2 Adhesion and Distribution of Epidiatomic Diatoms on Their Host
  - 9.3 The Specificity of Host-Epiphyte Interactions
  - 9.4 Cost-Benefit Analysis of Host-Epiphyte Interactions

- 9.5 Conclusion
- References

10 Towards a Digital Diatom: Image Processing and Deep Learning Analysis of *Bacillaria paradoxa* Dynamic Morphology

- 10.1 Introduction
- 10.2 Methods
- 10.3 Results
- 10.4 Conclusion
- Acknowledgments
- References

11 Diatom Triboacoustics

- 11.1 State-of-the-Art
- 11.2 Methods
- 11.3 Results and Discussion
- 11.4 Conclusions and Outlook
- Acknowledgements
- References

12 Movements of Diatoms VIII: Synthesis and Hypothesis[1]

- 12.1 Introduction
- 12.2 Review of the Conditions Necessary for Movements
- 12.3 Hypothesis
- 12.4 Analysis – Comparison with Observations
- 12.5 Conclusion
- Acknowledgments
- References

13 Locomotion of Benthic Pennate Diatoms: Models and Thoughts

- 13.1 Diatom Structure
- 13.2 Models for Diatom Locomotion
- 13.3 Locomotion and Aggregation of Diatoms
- 13.4 Simulation on Locomotion, Aggregation and Mutual Perception of Diatoms
- References

14 The Whimsical History of Proposed Motors for Diatom Motility[1]

- 14.1 Introduction[2]
- 14.2 Historical Survey of Models for the Diatom Motor
- 14.3 Pulling What We Know and Don’t Know Together, about the Diatom Motor
- 14.4 Membrane Surfing: A New Working Hypothesis for the Diatom Motor (2020)
- Acknowledgments
- References
- Appendix
- References

Index

Also of Interest

End User License Agreement

List of Illustrations

Chapter 1

- Figure 1.1 Drawing of a pennate diatom with two raphe branches on its valve.

Figure 1.2 Hypothesis that there is a point P between apices A1 and A2, so that the apical axis is tangential to the trajectory of P.

Figure 1.3 Traces of two trackers attached close to the apices of a diatom of *Navicula* sp.

Figure 1.4 Root-mean-square deviation of the angle between the apical axis and the smoothed trajectory of the point x located between the trackers.

Figure 1.5 Histogram of the frequencies of the angular difference between the direction of the diatom (apical axis) and the smoothed curve in P.

Figure 1.6 *Craticula cuspidata* observed from an almost horizontal view.

Figure 1.7 Hypothesis that there is a point P between apices A1 and A2, so that the diatom performs stochastic rotary motions around P.

Figure 1.8 Root-mean-square deviation of the transverse component of the fluctuations of the hypothetical pivot point.

Figure 1.9 The left side (a) illustrates the sequence of steps for reversal of direction, in which the tilting takes place after the direction of motion has been changed. In alternative (b), tilting takes place before reversing the direction.

Figure 1.10 *Craticula cuspidata* viewed from a horizontal perspective. The transapical axis is inclined against the substrate.

Figure 1.11 Trajectory of a diatom with reversal points. The point P never changes to a place of the raphe with opposite curvature.

Figure 1.12 Path of a diatom of the genus *Navicula* with reversal points. The direction of curvature changes at each reversal point.

Figure 1.13 Outline and raphe of a *Cymbella*.

Figure 1.14 Overlay of four images from a video showing a trajectory of a diatom of the species *Cymbella cistula*. The yellow line shows the trajectory of the leading apex. The line segment between the apices is marked in white.

Figure 1.15 On the left (a) the superimposition of images of a *Cymbella* rotating around a point near the helictoglossa is shown, on the right (b) a sketch of the diatom with raphe.

Figure 1.16 *Surirella biseriata* in valve view.

Figure 1.17 Trajectory of a *Surirella biseriata*. The driving side changes at the reversal points.

Figure 1.18 Paths of *Surirella biseriata* in a culture. They were visualized by overlaying frames of a video.

Figure 1.19 *Pinnularia viridiformis* with a length of approx. 90 µm.

Figure 1.20 Places within and on a biofilm where *Pinnularia viridiformis* can be found. The typical movement patterns are indicated by arrows. Shunting movements are marked with short arrows at both apices.

Figure 1.21 Superimposed frames of a video during the standstill of a diatom. A tension has built up in the biofilm.

Figure 1.22 *Nitzschia sigmoidea* on the water surface viewed with PlasDIC.

Figure 1.23 *Nitzschia sigmoidea* with a stereomicroscope in oblique view.

Figure 1.24 Sketch of a *Nitzschia sigmoidea* on the water surface seen from the horizontal direction.

Figure 1.25 Sketch of two adjacent *Nitzschia sigmoidea* on the water surface seen from the horizontal direction.

Figure 1.26 Very regular structure of a diatom cluster on the water surface (dark field).

Figure 1.27 Relative speed of two diatoms plotted versus their distance.

Figure 1.28 Energetically favorable patterns of three diatoms on the water surface: all diatoms parallel (a) and diatoms form a triangle (b).

Figure 1.29 Frequently observed movement patterns: movement along the raphe (a) and angular changes at connected apices (b).

Figure 1.30 Image sequence showing the temporal development of seven connected diatoms. The time between the first and last image is 170 seconds.

Figure 1.31 *Pinnularia gentilis*.

Figure 1.32 *Cymbella lanceolata*.

Figure 1.33 Two small colonies photographed with PlasDIC.

Figure 1.34 Elementary steps that contribute to structure formation.

Figure 1.35 Movement activity of diatoms between colonies.

Figure 1.36 Colonies at the beginning of intensive light irradiation (a) and after about two hours (b).

Figure 1.37 *Cymbella* culture in the light phase (a) and dark phase (b).

Figure 1.38 Number of free diatoms (blue) and the number of diatoms bound in colonies (red) over 24 days. A yellow bar indicates the phases of bright light.

Figure 1.39 Total number of diatoms (red) with exponential fitting (blue).

Figure 1.40 Number of diatoms in motion over the last 10 observation days.

Chapter 2

Figure 2.1 The polycarbonate channel used to image diatom motion, photographed on the stage of the inverted microscope. The depth, width, and length of the channel are 1 mm, 2 mm and 60 mm, respectively. A glass slide was bound to 2.5 mm × 7.5 mm polycarbonate block using two pieces of double-sided tape placed on the polycarbonate block. The coordinate origin coincides with the origin for the pixels. Diatoms move on the glass slide at the bottom of the chamber. The inset figure shows a schematic diatom, the coordinate axes, and the origin, in the plane of the top of the slide.

Figure 2.2 (a-b) Scatter plots of the simulated test object and the stationary polystyrene particle centroids, respectively. The stationary polystyrene particle was imaged at 821 fps. The number of points plotted is 1000 for the simulated particle and 4000 for the polystyrene particle.

Figure 2.3 Displacement histogram of the diatoms (symbols) and stationary polystyrene particle (continuous line) imaged at 821 fps.

Figure 2.4 (a) Plot of total displacement as a function of time in a diatom centroid measurement. The frames around the arrow are investigated in detail. (b) Overlay image of the diatom boundary for frames where the displacement was 293 nm at 1986 ms. White pixels show the overlapped points in the diatom boundary, while colors indicate change in boundary location; (c) and (d) show two consecutive frames of the diatom (diatom #2) for the displacement shown by an arrow in Figure 2.4 (a). The boundaries were calculated using the “Binary Centroid” algorithm. In b, green = frame c and magenta = frame d.

Figure 2.5 Angular velocity histogram of the diatoms #1-3 that were imaged at 821 fps. The diatoms exhibited changes in their orientation angles as they traversed the imaging strip horizontally.

Figure 2.6 In Figures 2.6a and 2.6c the orientation angle corresponding to the diatoms whose trajectories were previously investigated are shown (diatoms #2 and #3 in a and c, respectively). In Figure 2.6e the orientation angle of another diatom (diatom #4) is shown. Orientation angle is the angle between the major axis of the diatom and the x-axis. Figures (b), (d), and (f) are overlay images of the diatom boundary for different frames of the data shown in (a), (c), and (e), respectively. White pixels show the stationary points in diatom boundary, while colors indicate change in boundary location. An extra Gaussian smoothing was included in the image processing algorithm for the diatom #4, whose orientation angle is shown in Figure 2.6e. Otherwise, it was not possible to extract orientation data for diatom #4.

Figure 2.7 (a) The diatom in Figure 2.6d is rotated around the arc center of the white pixel region in Figure 2.6d; (b) the consecutive intersections of the major axis of the diatoms during rotation are shown as yellow dots. In (b), while the green dots at the centerlines are close to one another, they would coincide exactly if the rotation were precisely around the center of the diatom.

Figure A1 Displacement histograms of the image of the stationary polystyrene particle situated in the micromachined channel; (a) and (b) show x and y displacement histograms, respectively. Dots represent microscopy measurement while continuous lines are the Gaussian fits to the measurements. Two Gaussian terms are used for fitting total displacement data. The particle was imaged at 821 fps.

Figure A2 Fast Fourier Transform (FFT) of the x and y coordinates of the centroid location for the recordings made with the stationary polystyrene particle and a diatom; (a) and (c) are the FFTs of the x centroid data and (b) and (d) are the FFTs of y centroid data of the polystyrene particle and diatom #3, respectively. Prior to the FFT the centroid location mean was subtracted from the data.

Figure A3 Representative trajectories of the centroids of diatoms #1, #2, and #3 are given in (a), (b), and (c), respectively, over 500 frames. The diatoms were imaged at 821 fps.

Figure A4 Zoomed in views of the large displacements in the representative trajectories given in Figure A3. The plots (a), (b), and (c) show the centroids of diatoms #1, #2, and #3, respectively.

Figure A5 Mean square displacement (MSD) data of diatom trajectories. Diatom motion recordings were divided into segments that are 500 frames long and MSD data of each segment was calculated. The black dashed line represents the mean MSD and red line represents the best fit to the MSD for all diatoms (diatom #1 – (a), diatom #2 – (b), diatom #3 – (c)). All MSD data falls into the range shown by gray shaded areas in the figures.

Figure A6 Normalized velocity autocorrelation of all the diatoms (diatom #1 – (a), diatom #2 – (b), diatom #3 – (c)). The same trajectory segments as in calculation of diatom MSD data were used. All repetitions were used in calculating the autocorrelation.

Figure A7 The publicly available video [2.87] was analyzed using the SURF feature detection algorithm (please see the main text for the details); (a) displacement calculated in pixels as a function of the frame number; (b) the overlay of the features detected at frame numbers 422 (crosses) and 423 (circles). pts = points. Scale bar was not present in the original video.

Chapter 3

Figure 3.1 Vesicles carrying mucilage (black arrows) on sections of cells of *Pleurosigma* sp. near the girdle bands (a) and *Encyonema ventricosum* (b) in the area of areolae (TEM). Around the cells *Encyonema ventricosum* are visible fibers between the plasmalemma and the frustule and a dense layer of mucilage fibers on the surface of the frustule, however, the connections between them are absent. Chl - chloroplasts; m - mitochondrion. Scale – 200 nm.

Figure 3.2 The surface cells of *Nitzschia* sp. (a, b) and *Pleurosigma* sp. (c, d) after removal of frustules (SEM). At the tips of the precisely repeated contour of the frustules in the area of the raphe system of *Nitzschia* sp. in some cases separated fragments (arrows) are visible; it may be the place where the cell is firmly attached to the valve. The frustule of *Pleurosigma* does not have so extremely relief, but the contours of the cell here is very accurately repeated especially in the area of the raphe (arrows). It is possibly that most of the surface is not diatotepum, as this polysaccharide layer is very firmly attached to the leaf, which is very well illustrated by the *E. ventricosum* (Figure 3.1b). Scale: (a, d) – 10 µm; (b) – 5 µm; (c) – 1 µm.

Figure 3.3 Secretion of mucilage (arrow) through the raphe of the *E. ventricosum* (a) and vesicle (arrow), containing mucus near the raphe of *Pleurosigma* sp. (b) on ultra-thin cross sections (TEM) Scale: (a) – 200 nm; (b) – 500 nm.

Figure 3.4 Staining of actin microfilaments (phalloidin Alexa Fluor 488, green fluorescence) and nuclei (DAPI, blue fluorescence) in *Pleurosigma* sp. (a-b’) and *Nitzschia* sp. (c, d). Scale: (a, b) – 15 µm; (b’) – 5 µm; (c, d) – 10 µm.

Chapter 4

Figure 4.1 Morphology of an araphid diatom (a), *Staurosira construens* var. *venter* (scale bar: 2 µm) and a raphid diatom (b), *Navicula radiosa* (scale bar: 10 µm), diatom on valve view. The raphe (indicated by a white arrow) runs through the whole valve and is a primary structure for adhesion to surfaces and moving. (c) A close-up of the raphe (indicated by a white arrow) is shown (scale bar: 1

μm). (SEM images downloaded from diatoms.org with permission [4.107] [4.120] [4.143].)

Figure 4.2 Schematic of a benthic biofilm. Algae, predominantly pennate biofilms together with bacteria, protists, and fungi, are embedded within a protective matrix of extracellular polymeric substances (EPS). A benthic biofilm experiences high variability of spatial and temporal gradients of environmental factors such as inorganic nutrients, dissolved organic matter (DOM), and light. (Figure from Sabater *et al.* [4.129]. Reprinted under CC-BY license.)

Figure 4.3 A summary of some factors and gradients affecting diatom adhesion and motility on intertidal sediment. While adhering to the surface, cells sense their wettability through the production of intracellular nitric oxide (NO), which in turn mediates EPS production. Pennates generally have a preference for hydrophobic surfaces for attachment. Shear force or water flow affects substrate attachment with weakly attached cells easily dislodged by stronger shear. Once attached, the gliding capability and reversal control are mediated by the availability of extracellular and intracellular Ca^{2+}, respectively. As light only penetrates a few mm on the sediment, the substrate is divided into the photic and aphotic zone. Cells undergo diel vertical migration to the photic zone to photosynthesize on the surface with a taxa-specific temporal rhythm, thus leading to micro-niche segregation. Nutrient concentrations vary with depth, and motile raphids take up dissolved silicate (dSi) and phosphate (dP) on the aphotic zone as there are higher concentrations of these mineral nutrients with depth. The aphotic

zone also provides a protected and stable environment for vegetative and sexual reproduction. (Figure modified and redrawn from Saburova *et al.* [4.132] and adapted from Fenchel [4.59]. Reprinted with permission.)

Figure 4.4 (a) Scanning electron microscopy (SEM) images of EPS or mucilage trails and strands from the motile raphid diatom, *Navicula* sp. (scale bar: 5 μm). EPS trails were observed to be either straight or curved. (SEM images from Chen *et al.* [4.26]. (Reprinted under CC-BY license); (b) Adhesion of *Nitzschia palea* towards surfaces with different surface wettabilities (scale bar: 15 μm). Cells adhered more to hydrophobic surfaces after 4 hours. Insets are duplicate experiments. (Optical microscopy images from Laviale *et al.* Reprinted (adapted) with permission from Laviale *et al.* Copyright 2019 American Chemical Society [4.91]).

Figure 4.5 (a) A representative cell trajectory of *Seminavis robusta* showing the run-reverse motility of cells from high cell density experiments. (Cell track replotted from data from Bondoc *et al.* [4.15]). (b) The circular run-reverse gliding technique observed in *Nitzschia communis* under isotropic environmental conditions. Cells form arc-like runs with constant speed, reverse, and continue the arc-like runs in the opposite clock direction. Filled squares signifies the starting point of the cells. (Figure from Gutiérrez-Medina *et al.* [4.68]. Reprinted with permission.)

Figure 4.6 Motility of the model raphid pennate *Seminavis robusta* towards different stimuli across its life cycle. For every mitotic division, cells undergo size reduction until they reach a sexual

size threshold (SST). Cells can either continue to undergo vegetative growth or sexual reproduction to reconstitute their size and escape death. Throughout vegetative growth, cells require nutrients. Gradients of dissolved silicate (dSi) and phosphate (dP) elicited starved cells to accumulate at point sources within 5 and 20 min, respectively. Dissolved germanium (dGe) did not elicit any attraction, pointing to substrate specificity response. Meanwhile, starved cells also did not respond to gradients of dissolved nitrate or ammonium (collectively called dN). Once cells reach SST, they release sex-inducing pheromones (SIPs) that control the production of diproline (DPR) on MT^- cells. This pheromone is used by the MT^+ cells as a chemical guide on locating MT– spatially and pair with it. Sexual reproduction requires trace amounts of dSi for the reconstitution of the silica frustule of the initial cells. Additionally, SIP priming is essential for cells that recently crossed SST. On the other hand, critically small-sized cells can bypass the priming process and be readily attracted to diproline. This self-priming could be a self-preserving strategy for the cells to avoid extinction. (Figure from Bondoc *et al.* [4.16]. Reprinted with CC-BY license.)

Chapter 5

Figure 5.1 The effect of incubation time on *Stauroneis* response times in a mixed culture of *Craticula cuspidata* and *Stauroneis phoenicenteron*. This graph displays the average direction change response times for *Stauroneis phoenicenteron* cells in the presence of ca. 9:1 ratio of live *C. cuspidata: S. phoenicenteron* cells. *S. phoenicenteron* cells were isolated and washed from culture and

incubated together with *C. cuspidata* cells (C/S) in a 9:1 *C. cuspidata:S. phoenicenteron* ratio. Cells were then irradiated at their leading end with high irradiance (ca. 10^4 µmol/m^2s) 1s pulses of blue (470 nm) light, and observed to determine the time until they changed direction (response time). Response times significantly increased almost 2-fold from the initial incubation interval (0-10 min) within 20-30 min (30±2 µm/s and 57±7 µm/s respectively, P=0.003). Graphs represent the mean values of response times ± 1 SE. For comparison, unirradiated Stauroneis cell response times were 155±11 µm/s. Error bars represent ± 1 SE.

Figure 5.2 The effect of *Craticula cuspidata* or *Pinnularia viridis* presence on *Stauroneis phoenicenteron* response times. This graph displays the average direction change response times for *S. phoenicenteron* cells alone on slide chamber (Control). On a mixed slide chamber in a group by themselves (Isolated) or in a slide chamber in the presence of a high ratio of live *C. cuspidata* or *P. viridis* cells to *S. phoenicenteron* cells. Cells were then irradiated at their leading end with high irradiance 1s pulses of blue light, and observed to determine the time until they changed direction (response time). The presence of either *C. cuspidata* or *P. viridis* caused significant increases ($P < 0.03$) in cell response time from either control or isolated *S. phoenicenteron*. Error bars represent ± 1 SE.

Figure 5.3 The effect of culture medium on *Stauroneis phoenicenteron* response times. This graph displays the average direction change response times for *S. phoenicenteron* cells placed in the presence of culture medium in which either

S. phoenicenteron, *Craticula cuspidata*, or a mixture of *S. phoenicenteron* and *C. cuspidata* cells had been growing. Samples of the media were extracted, then briefly centrifuged in a microcentrifuge to remove any contaminating cells or cell debris. The *S. phoenicenteron* cells were then immersed into the desired medium, then isolated onto a slide chamber, allowed to incubate, then irradiated at their leading end with high irradiance 1s pulses of blue light, and observed to determine the time until they changed direction (response time). There was no significant difference between any of the treatment groups. Error bars represent ± 1 SE.

Figure 5.4 The effect of *Pinnularia viridis* on *Stauroneis phoenicenteron* response times. This graph displays the average direction change response times for *S. phoenicenteron* cells placed in two different areas of a cell chamber with differing proximities to *P. viridis*. This graph displays the average direction change response times for unirradiated *S. phoenicenteron* (Unirradiated), *S. phoenicenteron* irradiated in a slide chamber by themselves (Control), and *S. phoenicenteron* placed in a two-area slide chamber in which the entire chamber was subject to the same medium. Cells were irradiated at their leading end with high irradiance 1s pulses of blue light, and observed to determine the time until they changed direction (response time). The *S. phoenicenteron* in the two-area chamber were either in an area by themselves (Isolated), or in an area of the chamber where they were in close proximity to a large number of *P. viridis* (Live Pinn). In some trials the *S. phoenicenteron* were placed in

the presence of dead *P. viridis* (Dead Pinn) that had been killed by immersing the *P. viridis* cells for 30 sec in 95% ethanol prior to rinsing the *P. viridis* with distilled water and fresh diatom medium. The *S. phoenicenteron* cells in the presence of living *P. viridis* showed a significant increase in response time, even though they were exposed to the same medium as the isolated *S. phoenicenteron*. while those in the presence of dead *P. viridis* showed no such increase in response time. Error bars represent ± 1 SE.

Figure 5.5 Effect of *Craticula cuspidata* fixation method on repression of *Stauroneis phoenicenteron* direction change response time. *S. phoenicenteron* cells isolated and washed from culture were incubated together with *C. cuspidata* cells in a VALAP-spaced cell chamber where some *Stauroneis* were in contact with *Craticula* (grey bars) while other *Stauroneis* (isolated, solid bars) had no *Craticula* in near proximity. Stauroneis cells were then irradiated at their leading end with high irradiance flashes of blue light, and observed to determine the time until they changed direction (response time). *Stauroneis* in a mixed region with live *Craticula* had a significantly greater response time than *Stauroneis* in an isolated area ($P = 0.01$). This increase in response time remained when *S. phoenicenteron* were in the presence of *C. cuspidata* cells killed in ethanol or acetone fixation alone, but no significant difference in response time was observed when *C. cuspidata* were killed with a 50:50 acetone:ethanol mixture. The isolated *S. phoenicenteron* in the chamber also showed increased response times in the treatments containing ethanol or acetone fixed *C. cuspidata*.

Graphs represent the mean values of response times ± 1 SE.

Figure 5.6 Histogram analysis of *Stauroneis phoenicenteron* response times. The figure displays the distribution of direction change response times for *S. phoenicenteron* when in isolated groupings (a) or when in a mixed assemblage with *Pinnularia viridis* (b). *Stauroneis phoenicenteron* cells, when in the presence of P. viridis show some cells with control levels of rapid response times, along with a number of cells with greatly increased response times.

Chapter 6

Figure 6.1 Low-temperature scanning electron micrographs of diatom life styles (clockwise from top left): Stalked, tube forming, adpressed, epipelic. (Images: Irvine Davidson, University of St Andrews.)

Figure 6.2 Low temperature electron micrograph of the pathway of an epipelic diatom moving thorough fine silt (Bar marker = 10 um). (Image: Irvine Davidson, University of St Andrews.)

Figure 6.3 Top: Change in environmental driver (pressure) dependent on the presence of a “stabilizing biofilm” or under “regular erosion.” Bottom: Low-temperature scanning electron micrograph of MPB biofilm structure. (Image: Irvine Davidson, University of St Andrews.)

Chapter 7

Figure 7.1 Proposed model of the control of vertical migration by sediment-inhabiting benthic pennate diatoms, as responding to main directional environmental stimulus, light and gravity. The

figure illustrates the variation with the time of day of the diatom biomass at the sediment surface on samples kept in the dark (closed circles) and exposed to constant low light (150 µmol m-^{2} s-^{1}) during the subjective low tide period (open circles) (for more details, see [7.18]). Example of a day when the low tide takes place during the middle of the day. The gray horizontal plots represent the strength (bar thickness) of photo- and geotaxis, of negative and positive signal, along the day. (1) Upward migration starts before the beginning of the light period, driven by negative geotaxis. (2) Negative geotaxis ceases roughly at the time expected for start of the low tide light period: if no light is available at surface, the diatoms stop migrating upwards and the incipient biofilms start to disaggregate, due to random cell movement or weak positive geotaxis. (3) During light exposure, cell movements are controlled mainly by phototaxis, either positive (under low light intensities) or negative (under high light intensities). In the particular case of the data in the figure, positive phototaxis dominates, as samples were exposed to low intensity. (4) Anticipating the end of the light period, geotaxis becomes dominant over phototaxis, as cells begin to migrate downwards without any changes in incident illumination. Vertical gray areas represent periods of darkness. Vertical white area represents the period of light exposure (150 µmol m-^{2} s-^{1}) of the light exposed samples.

Chapter 8

Figures 8.1–8.13 LM images of *Eunotia* taxa in valve view (Figures 8.1–8.8) and girdle view, ventral-side up (Figures 8.9–8.11) to show variation in morphology and raphe shape and location (arrow in some images). (Figure 8.1 [8.28]) *E. bilunaris* (Ehrenb.) Souza – raphe recurved almost 180°. (Figure 8.2) *E. serra* Ehrenb. – raphe on valve face with slight curve toward apex. (Figure 8.3 [8.28]) *E. areniverma* Furey, Lowe et Johansen – raphe follows margin of apex from ventral to dorsal margin, and up onto dorsal mantle. (Figure 8.4 [8.28]). *E. pectinalis* var. *ventricosa* (Ehrenb.) Grunow (*E. pectinalis* var. *ventralis* (Ehrenb.) Hust. = synonym). (Figure 8.5) *E. bigibba* Kütz. – raphe with slight recurve. (Figure 8.6) *E. incisa* Smith ex. Gregory – raphe (not visible) only present on valve mantle (see Figure 8.17). (Figure 8.7) *E. muscicola* Krasske – raphe (not visible) on the valve face with slight recurve (see Figure 8.20). (Figure 8.8) Close up of valve apex and raphe of *E. bilunaris* in Figure 8.1. (Figure 8.9) *E. bigibba* and (Figure 8.10) *E. tetraodon* Ehrenb. – ventral-girdle view. Depth of valve only permits part of raphe to be in focus (on one plane) at a time. (Figure 8.11) Unknown valve in ventral-girdle view. Raphe almost all in focus. (Figure 8.12) Epiphytic cells of *E. bilunaris* (E) standing up on end from the mucilaginous sheath(s) of the cyanobacterium *Hapalosiphon* Nägeli ex Bornet et Flahault (Image credit R.L. Lowe). (Figure 8.13) SEM image of *Eunotia* on a bryophyte. For all images except for Figure 8.8: black scale bar = 10 μm. Figure 8.8: white scale bar = 5 μm. (Figures 8.1, 8.3, 8.4 originally published in Furey *et al.* [8.28] www.schweizerbart.de/journals/bibl_diatom).

Figures 8.14–8.22 SEM images of *Eunotia* taxa to show variation in morphology, along with external and internal raphe (R) shape and location on the valve face and valve mantle, helictoglossa (h), shape, location, and internal expression of the rimoportula (r), and external expression of the rimoportula pore (rp). (Figure 8.14 [8.28]) *E. areniverma* – raphe follows margin of apex from ventral to dorsal margin, and up onto dorsal mantle. (Figure 8.15 [8.28]) *E. areniverma* – internal view of apex. Rimoportula located mid apex. (Figure 8.16 [8.28]) *E. pectinalis* var. *ventricosa* – external view showing path of raphe from mantle onto valve face with slight recurve. (Figure 8.17 [8.28]) *E. incisca* – raphe located completely on valve mantle. External expression of rimoportula. (Figure 8.18) *E. bigibba* – curve of raphe onto valve face with slight recurve. (Figure 8.19) *E. serra* – raphe on valve face with slight curve toward apex. (Figure 8.20) *E. muscicola* – curve of raphe onto valve face with a slight recurve and (Figure 8.21) internal view of valve apex with rimoportula located close to the helictoglossa. (Figure 8.22) *E. serra* – internal view of valve apex with rimoportula located closer to dorsal margin. Scale bars as shown. (Figures 8.14–8.17 originally published in Furey *et al.* [8.28] www.schweizerbart.de/journals/bibl_diatom). [8.38] [8.53] [8.66], though their position could be derived if a more complex raphe system became reduced (discussed by Kociolek [8.44] and Siver and Wolfe [8.69]). Movement in eunotioid diatoms with their short raphe system, typically described as slightly (< 2 µm/sec [8.31]) or weakly motile (2 to 4 µm/sec [8.31]) (see eunotioid taxa in DONA [8.21] – Furey [8.26]), contrasts with that of more motile forms like naviculoid, nitzschioid, or surirelioid diatoms with more extensive raphe systems, typically described as moderately to highly motile. Examination of motility in *Eunotia* species may provide unique insight into motility in diatoms, especially for diatoms with more complex raphe systems. A search for the terms “motile” or “move” in florae focused on *Eunotia* (e.g., [8.20] [8.28] [8.48] [8.51]) and in >40 manuscripts with descriptions of *Eunotia* taxa new to science revealed little to no mention of motility. This chapter focuses on motility in the diatom genus *Eunotia*, but does not cover cellular or biomechanical details around the mechanisms of movement, as other chapters in this book discuss these aspects at length.

Figures 8.23–8.27 Schematic representation of some of the movement types for *Eunotia*. (Figure 8.23) Schematic of forward movement – apical displacement where cells tilt slightly so the anterior ends of the valves remain in contact with the surface and the posterior ends become slightly raised (**schematic modeled after Palmer [8.60] plate vi. fig. 2, and Bertrand [8.6] fig. 1**). (Figure 8.24) Valve in girdle view. (Each raphe branch labeled after Bertrand [8.6] (**see also Harbich [8.30]**). Black arrow following the line of the raphes on B to C apices represents diagonal line of direction, where the raphe on the C end becomes active. (Figure 8.25) Black horizontal arrow represents diagonal line of direction. Bidirectional arrow shows transition between raphes involved in forward motion (**schematic modeled after Bertrand [8.6], fig. 1**). (Figure 8.26) Schematic of a vertical polar pivot which can return a cell in girdle view, dorsal-side down (a) to ventral-side down (b,c) where a cell can then continue forward movement (c) (**schematic modeled after Palmer [8.60], plate vi. fig. 2, and Bertrand ([8.6], fig. 5]**).

(Figure 8.27) Schematic of a horizontal, polar pivot (a,b) to show direction of raphe activity (straight arrows, A and B). Note the cell is depicted ventral side up so the raphe branches are visible (rather than dorsal side up as the movement occurs). Curved arrows show direction of rotation. Dot represents the pivot point. (**Modified after images from Harbich [8.30]). See additional schematics in Bertand [8.5].

Chapter 9

Figure 9.1 Gliding cells of *Nitzschia sigmoidea* with stalked epiphytes of *Pseudostaurosira parasitica*: a single epiphyte in connective view (a), in valve view (b), and two epiphytes attached to the same frustule (c), which can be seen in movement [9.39].

Figure 9.2 Cells of *Nitzschia sigmoidea* with adnate epiphytes of *Fallacia helensis* (OM): single epiphyte in connective view and host in valve view (a), four epiphytes in valve view and host in connective view (b), which can be seen in movement [9.43].

Figure 9.3 Cells of *Nitzschia sigmoidea* with many epiphytes (OM): epiphytes of *Amphora copulata* on a still gliding host (a), epiphytes of *Amphora copulata* on a dividing host (b), epiphytes of *Amphora copulata* and *Pseudostaurosira parasitica* on the same host (c), which can be seen in movement [9.41].

Figure 9.4 Focus on epiphytes of *Nitzschia sigmoidea* (SEM). Adnate, *Fallacia helensis*, and stalked, *Pseudostaurosira parasitica*, epiphytes on the same host (a), two cells of *Pseudostaurosira parasitica* still associated after division (b), two superimposed cells of *Fallacia helensis* after

division and a third single one attached on the edge of the frustule (c), apex of a cell of *Pseudostaurosira parasitica* with the mucilaginous pad secreted for adhesion (d), individual of *Amphora copulata* (e) and internal view of one valve of *Amphora* sp., probably *Amphora copulata* var. *epiphytica* Round & Kyung Lee, considering the almost circular areolae on the ventral side (f). Scale bars indicate 10 µm, except in 9.4d (=5 µm).

Figure 9.5 Variations in the specific composition of epiphytes on *Nitzschia sigmoidea* between two sampling sites located on two connected rivers (up- and downstream sites), expressed as the occurrence of three epidiatomic species on frustules of *N. sigmoidea*. In fact, through the observation of fresh material, *N. sigmoidea* could not be strictly distinguished from the close species *N. vermicularis*. Both species were present in each site (see [9.44] for details).

Figure 9.6 Sigmoid frustules of *Nitzschia sigmoidea* (NSIO) and *Gyrosigma attenuatum* (GYAT) (OM, H_2O_2 treated material). Two species co-occurring in rivers samples with similar abundance, valve length and motility. However, *Gyrosigma attenuatum* was never seen with epiphytes.

Chapter 10

Figure 10.1 Drawing adapted from O.F. Müller (1783, translated in [10.54]), who was the first to characterize *Bacillaria* colonies. Examples 1 through 8 show the various states of expansion and contraction (dynamic phenotypes) of colonies.

Figure 10.2 *Bacillaria* close-up images of single cells using scanning electron microscopy (SEM). (a)

a whole valve seen from the inside. (b) close up of the same, middle section. The horizontal slit is the raphe. It lacks a central node. (c) Tip of the inside of a valve. (d) Middle section of a valve, exterior view. Note the raphe is a slit through the whole valve. (e): External view of the tip of a valve [10.33]. (Reprinted with permission of Amgueddfa Cymru, National Museum Wales.)

Figure 10.3 Demonstration of the image tracking procedure. (a) definition of tracked feature (white ellipse within a cell). (b) labeled (numbered) cells with relative measurements provided in red. The determined coordinates refer to a target in the middle of the template. The target can be moved and placed on the apex of the diatom being tracked. Then the coordinates of the apex are captured. This position is indicated in Figure 10.3a by a mark and a vertical line. Image scale: 38.36 μm per cm, or 0.325 μm per pixel. Scale bars 50 μm.

Figure 10.4 A diagram showing the five points on a sample cell (two ends, midpoint of the transverse line, and edges of the cell).

Figure 10.5 Point A is on the edge (vertical direction). The gradient direction is normal to the edge. Points B and C are in gradient directions. So, point A is checked with point B and C to see if it forms a local maximum. If so, it is considered for the next stage, otherwise, it is suppressed (set to zero). The result is a binary image with “thin edges.”

Figure 10.6 Diagram showing an example of hysteresis thresholding and the labeled edge relative to the “sure edge” threshold (V_{max}).

Figure 10.7 An example of feature identification performance for the Watershed Segmentation algorithm (left, red boundary) and Canny Edge Detection algorithm (right, white boundary). Image scale: 38.36 μm per cm, or 0.325 μm per pixel. Scale bars 50 μm.

Figure 10.8 An example of feature identification training (purple rectangles) for the deep learning approach on a single set of cells. Notice the resolution of the colony. An example of correct performance is shown in Figure 10.5. Image scale: 38.36 μm per cm, or 0.325 μm per pixel. Scale bar 50 μm.

Figure 10.9 Rank-order analysis of bounding box (cell) sizes (area) across the dataset. The area is measured in pixels squared. Image scale: 38.36 μm per cm, or 0.325 μm per pixel.

Figure 10.10 Rank-order analysis of height (blue) and width (red) of bounding boxes (cells) across the dataset. The area is measured in pixels squared. Image scale: 38.36 μm per cm, or 0.325 μm per pixel.

Figure 10.11 (Top) location of centroids in normalized coordinate space in selected dataset for static analysis. (Bottom) First two principal components from PCA analysis (PC1 represents horizontal position, while PC2 represents vertical position) of coordinates representing the *x,y* position for all four edges of each bounding box using the selected datasets for static analysis. Image scale: 38.36 μm per cm, or 0.325 μm per pixel.

Figure 10.12 An example of feature identification optimization procedures implemented in DeepLabv3. GRAY: no optimization applied, RED: Optimization #1, BLUE: Optimization #2. Given an initial number of training frames (y-axis), the non-optimized procedure (originally detected) will yield a certain number of boxes (x-axis). Applying various optimization procedures generally leads to a decreased number of boxes per frame for both low and high numbers of boxes.

Figure 10.13 Four examples of how the identified features map to two different images (a, c, e, g) of a *Bacillaria* colony. Points (b, d, f, h) represent the centroids for all bounding boxes identified in images a, c, e, and g, respectively. Image scale: 38.36 μm per cm, or 0.325 μm per pixel. Image scale: 38.36 μm per cm, or 0.325 μm per pixel. Scale bars 50 μm.

Figure 10.14 Three examples of how images of a *Bacillaria* colony are converted into a skeleton image. (Top Row) light microscopy images, (Middle Row) thin skeletonization based on a procedure implemented in GIMP, (Bottom Row) thick skeleton based on a procedure implemented in GIMP. Image scale: 38.36 μm per cm, or 0.325 μm per pixel. Image scale: 38.36 μm per cm, or 0.325 μm per pixel. Scale bars 50 μm.

Figure 10.15 Examples of relative movement of cells in a sample colony. (a) Comparisons between changes of position for cell #2 relative to cell #1 (red) and cell #3 relative to cell #2 (blue). (b) Comparisons between changes of position (red) and changes of velocity (blue) for cell #2 relative to cell #1. (c) a phase diagram of the data shown in b,